Investigating the impact of lattice induced strain on the magnetic properties of $NiFe_2O_4$ in ultra-thin films

Aadam Akbar

MSc

University of York
Physics

August 2022

Abstract

The magnetic ferrites are of signi cant interest in the eld of spintronics; being magnetic insulators and having a highly tuneable inverse spinel structure. $NiFe_2O_4$ has a multitude of applications across electronic devices such as in high frequency microwave devices, magnetic memory drives and spin lters. The high functionality of $NiFe_2O_4$ across microelectronics has resulted in a substantial increase in the number investigations into understanding its magnetic properties.

Induced lattice strain on $NiFe_2O_4$ via a substrate lattice mismatch has a profound e ect on the observed magnetic properties. This research aims to compare the e ects of tensile and compressive strains on $NiFe_2O_4$ and understand the in-plane and out of plane relationship on the changing magnetic properties. $NiFe_2O_4$ lms were consistently grown via PLD on three di erent substrates: Al_2O_3, MgO and $MgAl_2O_4$, each inducing a lattice strain of 12.13%, 0.76% and -3.36% respectively, with an average thickness of 11 nm. Characterisations of the magnetic properties were taken by VSM - producing hysteresis loops - and structural properties undertaken by XRD and TEM.

The results highlight the signi cance of the strain e ect, particularly in relation to the angular dependence of coercive and retentive properties. The $NiFe_2O_4$ lms were found to have in-plane emu/cc values of 200 on all three substrates. XRD data shows that $NiFe_2O_4$ was predominantly grown in the (222) plane and exhibited line broadening and peak shifts in accordance with the strain. TEM images show good single crystal growth and epitaxy on all three samples.

Contents

Abstract 2

List of tables 5

List of figures 8

Acknowledgements 9

Author Declaration 10

1 Introduction 11

1.1 Spintronics 11

2 Background and Theory 16

2.1 Literature Review 16

2.2 Crystallography of Spinel Structure 21

2.3 Magnetism in Solids 22

2.3.1 Magnetism in the ferrites 26

2.4 Magnetic Anisotropy 27

2.5 Domains 30

2.6 Hysteresis 31

3 Methodology 33

3.1 Pulsed Laser Deposition 33

3.2 Vibrating Sample Magnetometer 35

3.3 X-ray Diffraction 37

3.4 Transmission Electron Microscopy 40

3.4.1 Bright field dark field imaging 42

3.5 Sample Preparation 44

3.5.1 Mechanical Polishing 44

3.5.2 Focused Ion Beam 47

4 Results and Discussion 52

4.1 Nickel Ferrite 52

4.1.1 XRD 53

4.1.2 TEM 57

4.1.3 VSM 62

5 Conclusion 72

5.1 Future work 72

6 Bibliography 74

List of tables

1 Table showing the various $NiFe_2O_4$ K_1 values from literature at di erent thicknesses [77] [78] [79] [50]. 29

2 Table comparing the calculated d-spacing values from Bragg's law to the literature value [103]. 56

3 Shows the literature values of the molar mass, density and molar susceptibility for each substrate [104,43]. Using this data, the dimensionless value was calculated by equation 16. 63

4 Shows the comparative values of volume and molar susceptibility as calculated from experimental data in comparison to literature values. 64

5 The calculated sample volumes. Thicknesses determined via TEM and length and widths measured by a micrometer. 65

List of figures

Fig. 1 Schematic diagram of a spin valve consisting of two types of layered magnetic materials. 12

Fig. 2 The propagation of spin waves as the spin states realign in the direction of an applied field. 14

Fig. 3 Shows the lattice mismatch between the film and substrate, and subsequently, the induced compressive strain at the interface. 17

Fig. 4 Diagram showing a unit cell of inverse spinel $NiFe_2O_4$. Constituting of 32 O atoms (red), 16 Fe (gold) and 8 Ni (silver) [56]. 21

Fig. 5 a) Shows the tetrahedral positioning of the Fe atom (yellow) in relation to the O atoms (red). b) Shows the octahedral positioning of the B site from either cation in relation to the O atoms [57]. 22

Fig. 6 Diagram of the Bohr magneton; a magnetic dipole moment. 23

Fig. 7 Visual representation of Hund's first rule populating irons' 3d orbital, leaving 4 unpaired electrons contributing to the magnetic ordering. 24

Fig. 8 Diagram of the electron wavefunction interactions between the cations and anion in spinel structure. 27

Fig. 9 Diagram showing the structure of inner domains separated by Neel walls. . . 30

Fig. 10 Example of a typical M-H loop. 32

Fig. 11 Schematic diagram of a PLD chamber. 34

Fig. 12 Schematic diagram of the VSM setup. 36

Fig. 13 Birds-eye view of the sample normal (90°) to the applied field. 36

Fig. 14 Diagram showing incident x-rays reflecting off lattice planes in accordance with Bragg's law. 38

Fig. 15 Diagram showing the XRD shift and peak broadening on a strained lattice in comparison to an unstrained lattice. 39

Fig. 16 Diagram showing the signals emitted from different electron interactions with matter [95]. 41

Fig. 17 Schematic diagram showing which part of transmitted electrons are detected in Bright field and Dark field imaging. 43

Fig. 18 Shows the initial sample and the desired cuts via the diamond saw, after they have been removed from the glass slide. 45

Fig. 19 a) The creation of the epoxy resin glue with a test slide showing the dark orange colour. b) The specimen sandwiched and glued along the interface. . 46
Fig. 20 a) Shows the specimen sandwich ready to be polished. b) View of the sample in the optical microscope, indicating desired thinness. 47
Fig. 21 Diagram of the FIBSEM, showing the relationship between the two guns and the sample. 48
Fig. 22 a) The platinum deposition over the desired sample area. b) The trench digging process around the lamella. c) Image of the trimming process along the sides of the lamella, reducing the width. d) Shows the undercutting process to begin removal of the lamella. 49
Fig. 23 a) Attaching of the needle to the lamella. b) Shows a completely free lamella attached to the needle. c) and d) show the lamella welded onto the omniprobe grid, ready for thinning. 50
Fig. 24 a) Staggered thinning cuts used to achieve electron transparency. b) the nal lamella, under 100 nm wide ready for TEM analysis. 51
Fig. 25 Diagram showing the spectrum of induced substrate strains on $NiFe_2O_4$, based on the lattice mismatch with the chosen substrates. 52
Fig. 26 XRD graphs of grown $NiFe_2O_4$ lms on Al_2O_3, MgO and $MgAl_2O_4$. . . . 53
Fig. 27 (333) peak re ection of $NiFe_2O_4$ on $MgAl_2O_4$ substrate with respect to the theoretical value. 54
Fig. 28 XRD comparison plot between $NiFe_2O_4$ (222) lm peaks. 55
Fig. 29 Comparative XRD plot of the Mg substrate and the $NiFe_2O_4/MgO$ lm. . 56
Fig. 30 a) Cross-sectional high resolution TEM image of the $NiFe_2O_4/Al_2O_3$ interface. b) FFT of selected area from the lm. c) FFT of selected area from the substrate. 57
Fig. 31 a) FFT of a selected area from the $NiFe_2O_4$ lm from gure 30. b) The simulated di raction pattern of $NiFe_2O_4$ with zone axis [11-2]. c) FFT of a selected area from the Al_2O_3 substrate. d) The simulated di raction pattern of the Al_2O_3 substrate [0001]. 58
Fig. 32 a) Cross-sectional high resolution TEM image of the $NiFe_2O_4/MgO$ interface.b) TEM image of $NiFe_2O_4/MgO$ sample showing the interface and the atomic planes of the MgO substrate. 59

Fig. 33 a) FFT of a selected area from the $NiFe_2O_4/MgO$ lm. b) The simulated di raction pattern of $NiFe_2O_4$ with zonal plane [11-2]. c) FFT of a selected area from the $MgAl_2O_4$ substrate. d) The simulated di raction pattern of the MgO substrate with zonal plane [11-2]. 59
Fig. 34 a) Cross-sectional high resolution TEM image of the $NiFe_2O_4/MgAl_2O_4$ interface. 60
Fig. 35 a) FFT of a selected area from the $NiFe_2O_4/MgAl_2O_4$ lm. b) The simulated di raction pattern of $NiFe_2O_4$ with zonal plane [11-2]. c) FFT of a selected area from the $MgAl_2O_4$ substrate. d) The simulated di raction pattern of the $MgAl_2O_4$ substrate with zonal plane [11-2]. 60
Fig. 36 An example of raw VSM data from the $NiFe_2O_4/Al_2O_3$ lm. 62
Fig. 37 Raw VSM data, with converted units in emu/cc. The blue line shown is the line to be subtracted in order to determine the experimental value of Al_2O_3. 63
Fig. 38 a) The red line indicates the literature value of Al_2O_3 whereas the blue line is the experimental value to force saturation. b) Shows the resultant plot when the red line is subtracted from the initial raw data. 64
Fig. 39 a) The red line is an arbitrary line with a larger gradient that the experimental blue line.b) Shows the resultant plot when the red line is subtracted from the initial raw data a). 65
Fig. 40 Graphs a), c) and e) show the magnetisation hysteresis loops of $NiFe_2O_4$ taken from in-plane to out of plane, on three di erent substrates. Graphs b), d) and f) show the respective normalised plots for each substrate, in and out of plane. 66
Fig. 41 a) and c) Show comparative plots of the normalised in-plane and out of plane hysteresis loops respectively on all three substrates. Graphs b) and d) show the changes in loop shape and behaviour of the normalised in-plane out of plane hysteresis loops on all three substrates. 68
Fig. 42 Graphs showing the relationship between magnetic coercivity, remanence as a function of angle from 0°-90°on each substrate. 69
Fig. 43 Comparative graphs showing the strain e ect on the coercivity and remanence from in-plane to out of plane. 70

Acknowledgements

Firstly this work would not be possible without the support of my two supervisors Dr Vlado Lazarov and Dr Jing Wu who gave me the opportunity to produce this thesis. Furthermore, a special thanks to Dr Hari Vasili whose patience and guidance throughout proved invaluable, without you I would not be here. I would also like to thank Dr Jon Barnard and Dr Leonardo Lari for assisting me with learning new microscopy techniques.

I would like to acknowledge the support from within the rest of the physics research department, the Constantine College hockey team and my atmates who made my time in York so enjoyable. To *Voyna i mir* for accompanying me on this journey and no doubt greatly influencing my work. I am forever indebted to all the previous physics teachers in my life, they are the reason I am able to complete this work, for igniting my passion in physics and sending me on this quest for knowledge.

To my dear family and friends whose unwavering fidelity gave me the courage to persevere through all the delays and uncertainty over the last three years on this long and winding road. Their support throughout this process has been extraordinary and I am eternally grateful. Praise be to God.

Crucially, without the incredible commitment of all the key workers and NHS staff throughout the pandemic, the ability to perform such experimental work would not have been possible.

Author's Declaration

I declare that this thesis is a presentation of original work and I am the sole author. This work has not previously been presented for an award at this, or any other, University. All sources are acknowledged as References.

1 Introduction

The first discovery of a magnetic material was magnetite, in the form of a lodestone. The word magnet itself is derived from the region of Magnesia where these lodestones were found over 2800 years ago. These magnetite lodestones formed the basis of the magnetic compass, with the Chinese Han dynasty being the first to invent the compass around 200 BC, enabling them to expand their knowledge of the land and travel further distances [1]. For centuries the defining characteristic of this oblivious magnetic force was through navigation, allowing us to map the world and connect humanity through exploration. It was only in 1600 when Gilbert undertook serious investigations into the understanding of magnetic behaviour; concluding that the Earth itself is magnetic [2]. Nowadays we have learnt that the applications of this fundamental force are intrinsic in all aspects of life, with many animals detecting the magnetic properties of the Earth by magnetoreceptors for migration and navigation [3]. As we have rapidly improved our understanding of the natural world, we continue to delve deeper into the quantum origins of such phenomena. Investigating magnetic properties on the most fundamental level in ultra-thin films, is paramount to adding to our collective knowledge on such an important area in physics.

The magnetic materials being investigated in this thesis include magnetite (Fe_3O_4) and nickel ferrite ($NiFe_2O_4$). Not only do these compounds form very interesting and widely applicable ferrimagnets but are also magnetic insulators. Therefore, the magnetic ferrites are of great importance for spintronic applications and devices because they solely exhibit magnetic properties and not electrical ones. This is evident from the exponential increase in the number of research papers into the spinel ferrites [4].

1.1 Spintronics

The field of spintronics has become a big area of interest, fuelled by the discovery of the giant magnetoresistance effect (GMR), in 1988 [5]. This discovery bought the study of spintronics and spin transport into the fray of modern electronics, bringing innovations such as magnetic memory and data storage into computing. The discovery of GMR was awarded the Nobel prize in 2007, for its revolutionary applications of spin-based devices.

One of the biggest applications from the discovery of GMR was the spin valve (gure 1). A device intrinsic to applications for magnetic memory drives and data storage. Essentially a multi-layered thin lm; the combination of di erent magnetic materials allows the device to behave like a switch. Small applied elds can create di erent magnetisation alignments, either parallel of antiparallel, between the layers, which a ects the electrical resistance through the spin valve [6].

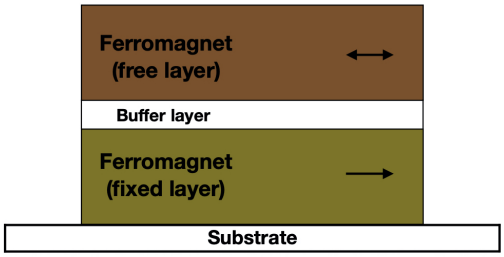

Figure 1: Schematic diagram of a spin valve consisting of two types of layered magnetic materials.

The aim of spintronics is to develop new data and logic devices, by adding an extra spin degree of freedom to the already well-established charge-based electronics. This brings about many advantages for future innovations, for faster and more energy e cient transistors. Figure 1 shows a xed ferromagnetic layer, whose magnetic orientation remains unchanged, and a free layer which can be manipulated by small magnetic elds. The current between the layers in (gure 1) - depends on the orientation of the free layer - provides far easier control for reading and writing information.

Exploiting the spin up or spin down states of electrons can produce devices with lower power consumption, far more compact components and with less volatility [7]. Spin valves, developed in 1995, have shown that it is possible to produce magnetocurrents, with relative changes of up to 400%, in small magnetic elds [8].

An important property of magnetic materials is the spin polarisation. The spin polarisation is the di erence between the density of spin up and spin down electron states in the solid, normalised by the sum of the densities (equation 1). Among the ferrites, Fe_3O_4 theoretically has a 100% spin polarisation at the Fermi level; (P=1) [9]. For Fe_3O_4, that would mean that all electrons at the

Fermi level i.e., electrons in the conduction band, will all have aligned parallel spin states.

$$P = \frac{N_{"}(E_F) \quad N_{\#}(E_F)}{N_{"}(E_F) + N_{\#}(E_F)} \tag{1}$$

$NiFe_2O_4$, the main subject of this thesis, is also of great interest with a variety of applications particularly in high frequency microwave devices [10].Moreover, by tuning its insulating properties, $NiFe_2O_4$ has been shown to be used in spintronic devices as a spin lter between layers, owing to its high tunnelling magnetoresistance e ect (TMR) [11].

TMR is a quantum mechanical magnetoresistance e ect which allows for the tunnelling of electrons through heterostructures called magnetic tunnelling junctions (MJT). MJT's consist of two ferromagnetic layers, separated by an insulating oxide barrier layer. In 1975, Julliere rst determined the existence the TMR e ect with a Ge based ller layer, showing the conductance through the MJT is dependent on the spin polarisation; the corresponding TMR ratio was calculated to be 14% [12]. Only electrons of the same spin orientation can tunnel through the junction into empty states, proportional to the density of states at the Fermi level, between the two ferromagnetic layers [13]. Equation 2 shows the TMR ratio as the di erence in polarisation between the two ferromagnets. Currently TMR ratios of over 400% have been established, at room temperature, using MgO [13].

$$TMR\ Ratio = \frac{2P_1P_2}{1 \quad P_1P_2} \tag{2}$$

Since spin is an intrinsic property of the electron, we can de ne spin currents in the same way as electrical currents, with the motion of electrons also transporting spin. These spin currents are the underpinning for realising the potential of spin-based devices, utilising the e ects of magnetoresistance.

The rst concept of magnetoresistance was introduced by William Thomson in 1857, upon his discovery that the change in direction of a magnetic eld a ects the conductivity across pieces of iron and nickel [14]. The description of such an e ect, known as anisotropy magnetoresistance (AMR), shows a relationship between the angle of applied magnetic elds and electrical conductivity. When a current ows parallel to the direction of an applied eld, the resistance increases; with the converse being true. Although generally the AMR e ect only has a small in uence over the electrical

resistance, there have been some experiments which have shown large scale e ects, of up to 50% [15].

Spin currents can also be de ned as an independent phenomenon to electrical current; as the propagation of spin via magnetic interactions without the motion of charge, the quantisation of the spin waves are known as magnons.

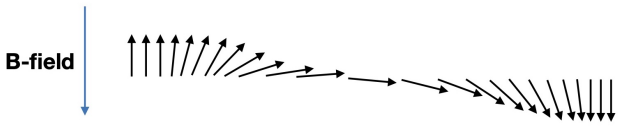

Figure 2: The propagation of spin waves as the spin states realign in the direction of an applied eld.

Semi-classically these spin waves are interpreted analogous to the electron spin precessing on its axis. The propagation of spin waves is due to the wobbling e ect of the precessing electron spin when interacting with a magnetic eld. The e ect of an applied eld will change the angle of precession (aligning of magnetic moments), this change will propagate through the material as a spin wave (gure 2). The magnons and their propagation are subject to thermal uctuations and damping e ects. The dynamics of electron spins is described by the Landau-Lifshitz-Gilbert equation (3). Where = $\frac{g_{\ o}}{h}$ and is the Gilbert damping constant.

$$\frac{dM}{dt} = \quad (M \quad H) + \frac{}{M_s}(M \quad \frac{dM}{dt}) \tag{3}$$

For a free electron in an applied eld, the single spin state will align with the eld. However, when correlated with the experimental observations of ferromagnetic materials, a relativistic damping term was included [16]. The damping force preserves the magnitude of spin and shows how the wobbling of the electron precession is continuous. This is a type of spintronics, based on magnon propagation, generation and detection, is known as magnon spintronics [17]. The transport of magnons through magnetic insulators has been shown to happen up to 40 m, further highlighting the applications of spin transport in devices [18]. Research has been done on $NiFe_2O_4$ to determine the extent of magnon transport and further spintronic applications [19].

More recently the discovery of the spin Seebeck e ect (SSE) in 2008 opened a new pathway for advancing research into spintronic devices [20]. The SSE generates spin currents via a temperature gradient which generates the propagation of magnons through ferromagnetic materials with a large

mean free path [21]. This generation of spin currents allows for thermal spin injection and propagation on macroscopic levels, far exceeding the spin di usion of conduction electrons [22]. The thermally induced spin currents can be injected into a non magnetic material, and, by virtue of the inverse spin hall e ect (ISHE), will be converted into a charge current [22]. Thus the SSE facilitates the conversion between spin-based and charge-based electronics. $NiFe_2O_4$ ultra-thin lms have been shown to exhibit the SSE and investigations have shown the profound signi cance of various growth properties on the observed e ects [23]. This shows the strong adaptability of $NiFe_2O_4$ to be manipulated for applications.

Speci cally, the investigation of thin lm ferrites is fundamental in observing new phenomena which are not present in bulk. With constant development of epitaxial growth techniques, we can grow consistent high quality ultra-thin lms. Having such ne control over the synthesis of the thin lms enables us to perform a focused analysis of the magnetic properties. This is particularly crucial for applications in electronic devices, to understand the plethora of e ects resulting from growth, such as antiphase boundaries, strain, and defects. Thin lm ferrites exhibit fundamental magnetic changes with properties such as coercivity, saturation and remanence being highly malleable to t the required application. With such a diverse set of applications within the eld of spintronics and microelectronics, the slightest deviation of magnetic properties can have profound e ects in industry.

This thesis aims to explore the e ects of di erent induced lattice strain on ultra-thin lm $NiFe_2O_4$ and determine the changes in magnetic properties. By improving our understanding of the behaviour of thin lm ferrites we can increase the e ciency of such devices and widen the scope of $NiFe_2O_4$ applications [24].

2 Background and Theory

2.1 Literature Review

The speci c aspect being investigated in this thesis is the e ects of epitaxial induced lattice strain on $NiFe_2O_4$; an e ect only prevalent in thin lms. The importance of lattice strain is not to be understated, with much greater demand for the manufacturing of microelectronics, there are profound implications of any properties which a ect the behaviour of such devices. These include devices such as multi-layer LC lters, multi-layer chip inductors and magnetic temperature sensors [25]. The quality of growth methods is intrinsic to the properties of thin lms, in fact the strain can even in uence the size of band gaps. There are always strains induced in the lms from deposition which can jeopardise the integrity of such devices. The consequences of stresses and strains in the structures need to be fully investigated, to control the speci c properties arising from the mismatch of the lattices of the substrate and the grown lm [26].

When growing a lm onto a substrate there will usually be a di erence in the lattice constants between the two unit cells (gure 3). This di erence in lattice constants is the mismatch, de ned by (4).

$$\frac{a_{sub} \quad a_{film}}{a_{film}} \tag{4}$$

To accommodate for the lattice mismatch, the deposited unit cells will distort its dimensions, to better t the lattice of the substrate. This will result in either a compressive or tensile strain. The strain is closely related to the lattice mismatch between the substrate and the incident lm growth. Strain is similarly de ned as (5) [27].

$$= \frac{a_{sub} \quad a_{film}}{a_{sub}} \tag{5}$$

Furthermore, strained systems can be accentuated by the e ects of thermal strain, deriving from di ering heat capacities and thermal expansions of the two compounds at the interface. This leads to the question of how far can a unit cell be strained? There is an elastic limit to which the cell

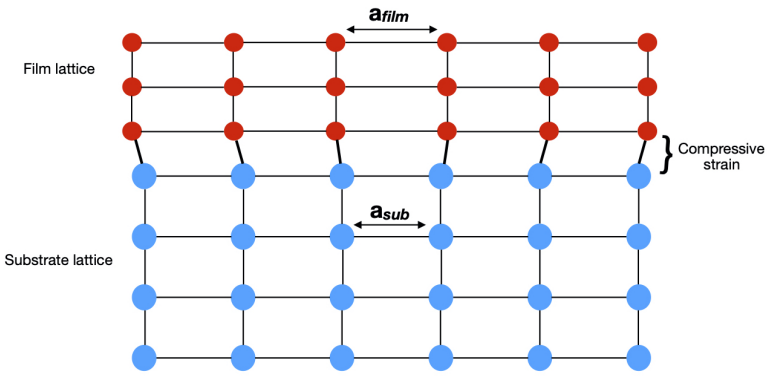

Figure 3: Shows the lattice mismatch between the lm and substrate, and subsequently, the induced compressive strain at the interface.

cannot exceed and also a certain critical thickness, at which point the strain will be released by the system, resulting in crystal defects and dislocations [27]. There are several mechanisms of relaxations which are heavily dependent on the type of strain and temperature, such as di usion creep and dislocation glides [28]. Ultimately strain relaxation is responsible for mass structural changes, inherently a ecting the transport properties and the stability of such lms [29].

There has been a lot of interest across literature to quantify the full extent of substrate induced strain on the magnetic properties in the ferrites. Indeed, with a plethora of physical interactions it can be di cult to attribute the speci c e ects of lattice mismatching to the magnetic properties. A mathematical analysis from rst principals into the strain e ect, by (Fritsch and Ederer, 2011), concluded that there is a signi cant impact on the magnetic anisotropy in thin lms [30]. The anisotropy of a magnet is a term to denote the preferred direction of a magnetic materials' magnetisation; this will also in uence other magnetic properties. Changes in magnetic anisotropy can arise from structural defects, stoichiometry changes and the distribution of cations in the cell. Additionally, there are also contributions to the strain from the formation of antiphase boundaries (APB) in thin lm spinel growth. These boundaries are a speci c type of defect, formed by the breaking of symmetry through the process of growth; forming the divide between two grains [31]. APB's are substrate dependent and the magnitude of lattice strain will induce varying sizes of APB's.

A study by (Datta et al., 2010) sought to investigate these e ects, showing that the signi cance of APB's decrease with the less strain inducing substrates. Furthermore, there is a knock-on e ect,

with an observed increase in magnetic saturation with closely matched substrates [32]. APB's have been of particular interest in literature due to their impact on the spin transport of Fe_3O_4 across these boundaries [33]. A comparative piece by (Singh et al., 2017) between certain substrates and the formation of APB's reveals observed shifts in the saturation eld values [34]. Furthermore (Singh et al., 2017) demonstrates it is possible to produce APB free $NiFe_2O_4$ on closely matched substrates; underpinning the strong relationship between strain and APB's.

Further experimental investigations have shown that epitaxial strain, speci cally at the interface, is a considerable factor in changing magnetic properties. From (Dhakal et al., 2010) there is a correlation between the size of the lattice strain and the observed changes in anisotropy via hysteresis M-H graphs [35]. A recent paper (Liu et al., 2021), shows speci cally that strained $NiFe_2O_4$ grown on $SrTiO_3$ exhibits changing coercivity and remanence values, from in-plane to out of plane with respect to the applied eld [36]. Similarly, the magnetoresistance of the thin lms has been determined to also be strain dependent [37]. It has been comprehensively shown by (Li et al., 2019) that the changes in magnetic anisotropy of $NiFe_2O_4$ result in signi cant impacts on the SSE [38].

An important phenomenon due to induced stains is the magnetostriction e ect. The magnetostriction of a magnetic material is the characteristic, that in an applied eld, there will be a reversibly induced change in dimensions of the unit cell. Applying a magnetic eld instigates a redistribution of small domain structures, aligning them along the magnetic easy axis. As a result, this gives rise to a macroscopic strain e ect [39]. For $NiFe_2O_4$, the magnetostriction coe cient at saturation has been determined to have a negative value along the easy axis: $_{(111)} = 21.6\text{x}10^{-6}$ at 293K [40]. Most importantly, the inverse magnetoelastic e ect, is the cause of changing magnetic properties.

The concept of structural magnetoelasticity of materials has gained interest as a phenomena symbiotic with substrate induced strain, further accentuating changes in magnetic characteristics, in accordance with the stress in icted on the sample. Strain on its own can even be manipulated further as an extra degree of freedom in spintronic devices [41]. The magnetic energy is coupled with the elastic properties of the crystal lattice such that, the strain produces a change in the crystal bonding angle, facilitating a di erent exchange mechanism. The magnetostriction caused by induced strains, a ects the equilibrium position of the samples' magnetisation; this new direction can be determined by the summation of the external eld and the strain induced eld [42].

Literature shows there is a signi cant e ect on hysteresis properties of magnetic materials resulting from epitaxial strain and a high demand for further investigations into the eld. It is most appropriate to compare the holistic magnetic data via the magnetisation per cm^3 (emu/cc). In bulk $NiFe_2O_4$ this has a value of 330 emu/cc at room temperature [43]. There are a wide range of reported emu/cc values of thin lm $NiFe_2O_4$, with some papers observing results close to bulk and others reporting results above and below the bulk value. Singh et al., 2017 shows that $NiFe_2O_4$ lms re ect bulk like emu/cc for substrate induced strains between 0.2% - 3.1%, whereas Li et al., 2012 reports smaller values [34,44]. However, these values are derived from polycrystalline lms with thicknesses exceeding 450nm, which can be in uenced by strain relaxations. A study performed by Huang and Ding, 2013 on Fe_3O_4 with di erent induced lattice strains concludes that the e ect produces varying values of emu/cc compared to bulk [45]. Some papers even report that nanoparticles of $NiFe_2O_4$ have values of emu/cc almost half of bulk material [46]. Most relevant to the work done in this thesis, Venzke et al., 1996 shows that ultrathin $NiFe_2O_4$ lms were observed to have an M_s value of 190 emu/cc [47]. From these papers we can determine that the emu/cc values are expected to decrease from bulk as a function of lm thickness. Concluding from literature, it is unclear to what extent strain impacts the emu/cc values in ultra-thin lms as there is little information with consistent thicknesses along with the varying densities of APB formation.

As well as magnetic characterisations, XRD is an essential tool used to determine the extent of strained lms. Strained systems show a shift in XRD peak relating to the change in dimensions of the unit cells. Papers such as (Ma et al., 2010) show that with the likes of thermally induced strain there is an observed shift in XRD peaks [48].

Although the strain e ect is prevalent within all the ferrites, we note that it is particularly dominant in $CoFe_2O_4$ [30]. Due to crystal eld theory and the population of the split 3d energy levels, $CoFe_2O_4$ has a much stronger magneto-crystalline anisotropy (MCA) [49]. The stronger directional dependence of $CoFe_2O_4$ is responsible for the stronger magnetoelasticity it exhibits over the other ferrites. The deformation of the $CoFe_2O_4$ lattice results in a larger change in magnetisation by comparison. As a result, $CoFe_2O_4$ has been the main focus of strain related experimentation in literature rather than $NiFe_2O_4$ and Fe_3O_4. With regards to $NiFe_2O_4$, there is a lack of research further investigating epitaxial strain in $NiFe_2O_4$, partially due to its complex crystal structure and therefore a reduced number of suitable substrates [50]. The most common substrates chosen for $NiFe_2O_4$ growth are MgO, $MgAl_2O_4$, $SrTiO_3$. Mainly due to the close lattice match of MgO and the spinel crystal structure of $MgAl_2O_4$. Each of these substrates have their drawbacks, with MgO

having an incompatible rock salt structure and $MgAl_2O_4$ having a higher lattice mismatch.

Due to the profoundness of the strain effect, it can be investigated in many ways, such as a function of film thickness. By undertaking continuous magnetic measurements at varying film thicknesses, (Soffin et al., 2015) concluded that there are large changes in magneto resistance measurements and that strain relaxations up to the critical thickness influence the APB density districation [51]. Thermal induced strain is also well researched. These two aspects of strain are most prevalent in literature, yielding very distinct changes in hysteresis properties, from inverse spinel systems, in particular $CoFe_2O_4$ [52]. Highly relevant work has been done on $CoFe_2O_4$ by (Huang et al., 2006), indicating that the film behaviour is strongly influenced by the lattice mismatch [53]. Additionally (Huang et al., 2006) reports characteristics from both tensile and compressively strained substrates backed up with hysteresis data and notable XRD peak shifts.

This work aims to demonstrate how magnetic properties in $NiFe_2O_4$ change from being grown in compressive to tensile strain induced by different substrates. Keeping thickness and temperature constant to isolate the effects of induced epitaxial strain and solely relating them to lattice mismatch and APB formation.

2.2 Crystallography of Spinel Structure

The ferrites crystallise in a spinel structure; typical of transition metal oxides, taking the form AB_2O_4 (gure 4). Spinels form in a close packed cubic structure with the anions (oxygen) populating face centred cubic (FCC) lattice points. In a normal spinel structure the atomic sites A and B are populated by the cations; B sites being occupied by trivalent cations B^{3+} and A sites by bivalent cations A^{2+} . In relation to oxygen atoms, atom A is situated on tetrahedral sites and atom B on octahedral sites (gure 5). These tetrahedral and octahedral sites are referred to as the cation sublattices [54]. There are a variety of metal cations able to populate the A and B sites, depending on electronic con guration and ion radius, making spinels a very versatile crystal structure [55]. Due to the multiple atomic sites, the unit cell of a spinel compound is formed by a combination of 8 FCC cells. Depending on the constituent elements in the spinel stricture and growth method there can be di erent phases of spinel compounds such as inverse and partially inverse spinels. $NiFe_2O_4$, studied in this thesis forms an inverse spinel structure, denoted by $B_{tet}[AB]_{oct}O_4$ (Fe^{3+} $[Ni^{2+}Fe^{3+}]O_4$), where the cations populate di erent sites in the crystal. For inverse spinels, the octahedral site is randomly populated by both A and B cations. The physics of electronic interactions and the subsequent magnetic properties of the spinels are heavily dependent on their structure.

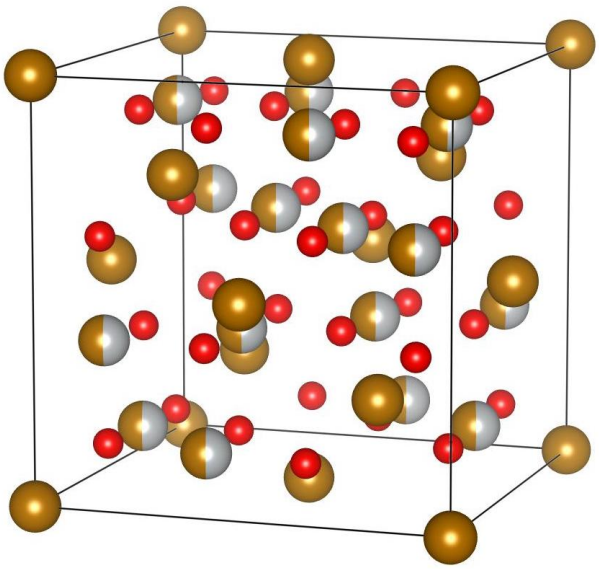

Figure 4: Diagram showing a unit cell of inverse spinel $NiFe_2O_4$. Constituting of 32 O atoms (red), 16 Fe (gold) and 8 Ni (silver) [56].

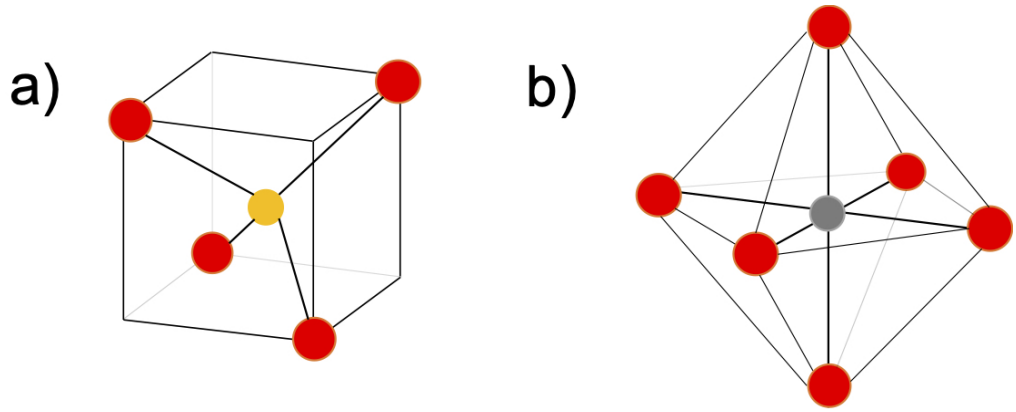

Figure 5: a) Shows the tetrahedral positioning of the Fe atom (yellow) in relation to the O atoms (red). b) Shows the octahedral positioning of the B site from either cation in relation to the O atoms [57].

2.3 Magnetism in Solids

Although the phenomena of magnetism has been utilised since the ancient Greeks in 800 BC, the atomic theory of magnetism has only recently - in the 20^{th} century - been fundamentally understood, by the formulisation of quantum mechanics, electromagnetism and the discovery of electron spin [58]. Before quantum theory, the macroscopic e ects of magnetism had been well documented by the likes of rsted, Faraday, Ampere and Gauss, but the underlying mechanisms still eluded them. By 1900 it was well established that magnetism, and the resultant magnetic forces, are produced by the motion of charged particles.

In atomic structure there are two sources of magnetism, one emanating from the orbital magnetic moment and the other from the spin magnetic moment. The idea of an electron orbital moment was put forward by Bohr, describing a semi-classical model of allowed orbitals, quantised in h (gure 6). This de ned the concept of a magnetic dipole moment and the fundamental unit of electron magnetism, the Bohr magneton (6). Initially, this orbital e ect was believed to be the sole reason behind atomic magnetism, but this model still had many de ciencies [59]. It took until 1925 for the existence of electron spin to be postulated by Uhlenbeck and Goudsmit and was not widely accepted until 1928 [60]. This laid the foundations for deeper investigations into the origins of magnetism.

$$_B = \frac{eh}{2m_e} \tag{6}$$

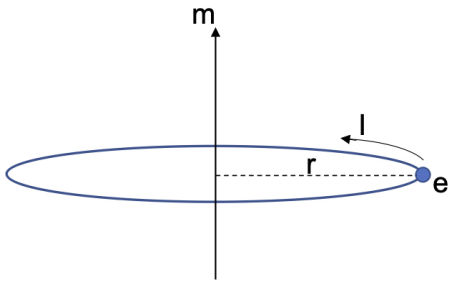

Figure 6: Diagram of the Bohr magneton; a magnetic dipole moment.

The interaction between these two sources of magnetic moments forms the backbone for macroscopic magnetism in solids. All solids exhibit some magnetic properties when placed in an applied field - usually by diamagnetism - such that an electric current will be induced in a material to oppose the external magnetic field; classically explained by Lenz's law. However, diamagnetic susceptibility is incredibly weak and not the product of any intrinsic ordering. The more intriguing magnetic properties cannot be explained classically but require a quantum approach.

From an atomic point of view, we can understand the magnetic ordering of elements by understanding their electronic structure. Atomic orbitals are derived from solutions to the Schrödinger equation, giving spherical harmonic solutions, for the probability of finding a bound electron in each orbital. These solutions are related to specific quantum numbers governing each degree of freedom, from the intrinsic spin magnetic moment (m_s) to the orbital angular momentum (m_l). Spontaneous ordered magnetism can be holistically understood from these spin and orbital interactions. Each atomic shell is populated by a certain number of electrons, according to the allowed orbitals. For a filled shell (an even number of electrons), the orbital magnetic moment will be zero, because the relationship between the magnetic and orbital quantum numbers cancel all moments. Qualitatively we can understand this as the electrons reducing the Coulomb interaction between each orbital. Semi-classically, if all electrons orbit in the same direction there is less spatial overlap between the wavefunctions, reducing their coulomb interactions. The spin contributions will also be zero as there are an even number of paired spin states. Hence, only electronic configurations with unfilled states will exhibit magnetic properties. These atoms with unfilled states show paramagnetic behaviour. Paramagnetic crystals show no long range ordering and only exhibit magnetic properties when placed in an applied field. Furthermore, they retain no long term effects from being magnetised, due to thermal fluctuations in the lattice.

To determine the net magnetic moments of atoms we have to understand how these states are populated. They are determined by Hund's rules [61]:

1. Each orbital is populated such that the total spin moments, S are maximised. Therefore, all orbitals are singly occupied before doubly occupied.
2. The orbital quantum numbers are chosen so that the maximum value of the angular momentum, L is achieved.
3. The total magnetic moment is calculated depending on whether the shells are less than half filled, J=L-S or more, J=L+S.

Hund's rules are paramount for understanding the mechanisms responsible for long range magnetism, particularly the first rule. Maximising the multiplicity of spin states is due to the exchange interaction and a consequence of the Pauli exclusion principle (figure 7). The exchange interaction dictates that is energetically favourable for electrons spins to align parallel. Antiparallel electron spin pairs mean that there would be more overlap between their wavefunctions; being in the same orbital. By firstly populating the electrons in different states, it results in less spatial overlap and thus a smaller coulomb interaction, making this the lowest energy level in the system. This is an intuitive approach but is not always the case, mainly the effect is due to less screening of electrons in higher multiplicities, giving the nucleus-electron potential more effect [62]. The exchange interaction is only partially due to the coulomb interaction and can be more appropriately described as a transition mechanism between two differing energy states. There is no classical equivalent to the interaction, a purely quantum mechanical phenomenon.

For the iron group elements the 3d orbital holds 10 electrons; the electronic configuration of Fe and Ni are as follows:

- Iron $1s^2 2s^2 2p^6 3s^2 3p^6 4s^2 3d^6$
- Nickel [Ar] $3d^8 4s^2$

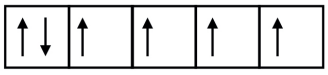

Figure 7: Visual representation of Hund's first rule populating irons' 3d orbital, leaving 4 unpaired electrons contributing to the magnetic ordering.

$$E_{exchange} = \quad 2J_{ij}S_iS_j \tag{7}$$

The exchange interaction from Hund's first rule is the driving force behind ordered magnetism, ensuring the unpaired electron spins are all parallel, but without any contribution from the orbital magnetic moment. For the iron group (Fe, Co, Ni) which are ferromagnetic, there is a quenching of the orbital moment such that J=S; only spin contributes to the macroscopic field. This is a consequence of crystal field theory; in how the solids are ionically bonded together through electronic charge. Depending on the strength of these bonds compared to the total spin-orbit coupling, the orbital magnetic moment can be quenched [63].

Crystal field theory (CFT) is a bonding model of transitions metals, that describes its bonding with other atoms, known as ligands. These ligands act as electron donors to the central metal ion to form the crystal lattice, in this case, oxygen. CFT is essential in determining magnetism in solids, by affecting the degeneracies of the 3d orbitals. When the oxygen atoms donate electrons into the metal ions orbitals, they repel the other 3d electron orbitals, creating different energy states [64]. As a result this causes a splitting of the energies of certain 3d orbitals, known as the crystal field splitting energy. The magnetic behaviour of the resulting compound will depend on the size of this splitting energy as it changes the electronic configuration.

Therefore the unpaired spin moments in the 3d valence band for Fe, Co and Ni atoms are responsible for ferromagnetism. Why these transition metals exhibit ferromagnetism and the others do not is due to the specific 3d itinerant electrons, their localisation and the strength of the intra-atomic exchange interaction [65]. Fe, Co and Ni each have few enough 3d electrons such that there is a strong exchange mechanism but are still localised [64]. Along with the 3d electrons, the 4f electrons of the lanthanides are also ferromagnetic.

Despite the effects of entropy, the magnetic system remains ordered to high Curie temperatures; 858K for Fe_3O_4 [66]. After the Curie temperature the material becomes demagnetised until the temperature is lowered.

2.3.1 Magnetism in the ferrites

The magnetic ferrites exhibit very di erent properties and applications than that of pure ferromagnets, due to their indirect exchange mechanism. This so-called superexchange interaction was formulated in 1934 and fully theorised by Anderson to understand the e ects of antiferromagnetism in metal oxides [67]. The superexchange principle di ers from the ordinary magnetic exchange interaction due to the constituent atoms making up the crystal structure. In pure magnetic metals - with no dopants - the direct exchange interaction is strong, whereas in the ferrite's there is a relatively large gap between the cations and importantly the unit cell is populated by oxygen atoms, a non-ferromagnetic element.

These oxygen atoms facilitate the magnetic exchange, populating orbitals based on Hund's rules [68]. This property of the transition metal oxides weakens the direct exchange mechanism and determines their ferrimagnetic nature. Speci cally, the inverse spinel structure plays a critical role in the superexchange interaction.

The origins of ferrimagnetism in the spinels were rst investigated by Louis Neel in 1948; concluding that the magnetisation is equal to the sum of the moments from the cations sublattice's [69]. The relationship between the tetrahedral and octahedral sites has a strong in uence on the observed magnetic properties, with the most signi cant interactions occurring between the A-B sites. This interaction produces a negative exchange interaction, resulting in the di erent cations sublattices having antiparallel orientated spins [70]. However, with unequal populations of identical cations in the structure; the B sites dominate (there are twice as many). Therefore, the net moment of aligned spins yields ferrimagnetic ordering. Although there are other interactions between the cations, such as A-A and B-B, their e ects are negligible and are up to ten times weaker than the dominant A-B exchange [71].

Superexchange is speci c to localised 3d orbitals separated by 2p orbitals in metal oxides. For example, in the case of two closely packed magnetic cations separated by an anion, the half- lled d orbitals will overlap with the un lled p orbital from the anion (gure 8) [72].

The overlap of the orbital clouds allows for electron hopping between the two cations. This e ect is geometrically dependant, and the strength of the exchange mechanism changes based on the symmetry of the system [73]. This interaction gives rise to a transfer e ect between the cation's

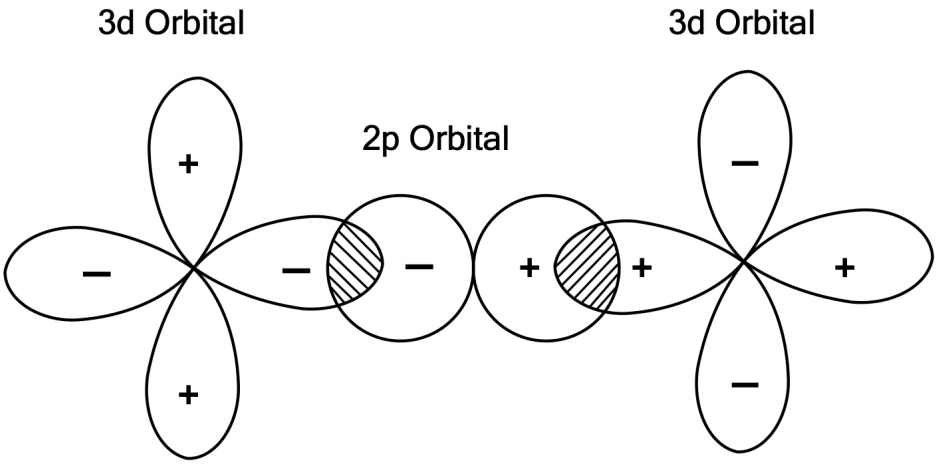

Figure 8: Diagram of the electron wavefunction interactions between the cations and anion in spinel structure.

outer electrons, occurring with antiparallel spins, for the lowest energy state. As well as the intermolecular distances, the constituent basis of the spinel structure plays a big role with the overlap; the effect being more significant for the trivalent cation, in this instance Fe. The effects of differently populated 3d orbitals in the structure, such as Co or Ni, can be estimated to derive the magnetic strength of the spin alignments [72].

2.4 Magnetic Anisotropy

In thin films there are three main types of anisotropy contributions. These are magneto-crystalline (MCA), shape and strain anisotropies, which determine the directional dependence of the magnetic moments in a crystal.

The MCA is intrinsic to the nature of the specific crystal, showing a clear easy axis of magnetisation. The origins of this effect is due to the crystal structure. For example, in a cubic lattice with lattice constant a, the atoms in the (100) and (010) directions will exhibit the same anisotropy, as the distances are constant. However in the (111) plane, the distance between the atoms will now be $\frac{p}{2}a$, thus resulting in the hard axis of magnetisation. The larger distances between the magnetic

moments means less magnetic interactions, requiring higher energy. This will mean that a larger applied eld is required to achieve magnetic saturation along the hard axis. Depending on the space group and structure, the direction of the easy axis changes. Furthermore, the larger the inherent MCA the larger the coercive eld.

Shape anisotropy is the magnetic dependence on the physical shape of the material and is a consequence of its demagnetisation eld (H_d); which opposes the applied eld [74]. Bulk $NiFe_2O_4$ has its easy axis along the (111) direction, but as the sample gets smaller the out of plane magnetisation direction - for (111) grown lms - becomes too energetically costly to maintain. Reducing the internal demagnetisation eld in-plane, massively reduces the external stray eld. Therefore, the shape anisotropy makes it easier to magnetise the sample along its longer axis [75]. The geometry of the sample a ects the direction of the internal demagnetisation eld and reduces the total magnetic energy of the system. In thin lms, the shape anisotropy contribution becomes more prominent as the sample gets thinner.

For a spherical sample there would be no shape anisotropy as the symmetry has no preferential direction and will magnetise in any direction. From bulk to thin lm, there is a critical thickness where the shape anisotropy overcomes the inherent MCA to dominate the directional dependence.

Taking the opposing H_d eld we can write the expression for the magnetic ux inside the magnet as:

$$B = H_d + 4 M \tag{8}$$

Equation 8 shows that H_d can never exceed $4 M$.

The strain contribution to anisotropy - magnetoelasticity - is proportional to the deformation of the lattice. The elasticity of the lattice is coupled with the magnetic properties.

The total contributions to the magnetic anisotropy can be calculated by adding the MCA, shape and strain anisotropy respectively (9).

$$H_A = \frac{2K_1}{M_s} + 4 M_s + H \tag{9}$$

H_A is a measure of the required eld to overcome the easy axis alignment of the moments; where

K_1 is the anisotropic constant and M_s the emu/cc value at saturation. Equation 9 is used for uniaxial anisotropy, where there is a clearly de ned easy and hard axis. Moreover the values of K_1 can be further used to calculate the magnetocrystalline anisotropy energy (MAE). The MAE is expressed in the form of a series expansion, but since the rst K_1 term dominates it can be simpli ed into the following equation [76]:

$$E_A = 2K_1V\sin^2 \tag{10}$$

Where V is the volume of the sample and is the angle between the magnetisation direction and the easy axis. Table 1 shows the comparative values of the anisotropy constant (K_1) for di erent thicknesses of $NiFe_2O_4$. However, it is di cult to accurately compare the anisotropy constants, as there is no clear consensus from literature and values can be volatile, depending on conditions [75].

	Bulk (10mm)	Thin lm (450nm)	Ultra-thin lm	Nanoparticle (19nm)
K_1 (erg/cc)	$4.2x10^5$	$6.2x10^4$	$12.7x10^6$	$3.3x10^4$

Table 1: Table showing the various $NiFe_2O_4$ K_1 values from literature at di erent thicknesses [77] [78] [79] [50].

2.5 Domains

Magnetic materials do not exist in uniformly aligned states; that is to say a ferromagnetic substance will not achieve magnetic saturation without the presence of an applied magnetic field. Such long ranged ordering cannot be solely sustained by the exchange interaction and is destroyed by entropy. To holistically describe the nature of magnetism, Pierre Weiss investigated the presence of magnetic substructures, leading to the development of Weiss theory in 1907 [80].

In real magnetic solids the spin ordering is only uniform in specific regions of the solid called domains. A piece of ferrite is spontaneously divided into many magnetic domains (figure 9), in order to minimise the demagnetisation/stray field. This is the most energetically favourable state for the system and, it is subject to the constraints of the anisotropy contributions [43]. The spin-orbit interaction is responsible behind such ordering; when the spins are realigned the orbital moment - which has a strong interaction with the lattice - resists the change [81]. There is an inherent anisotropic energy required to overcome the spin-orbit coupling to shift domains. Each of these domains have different directions of magnetisation and are split by domain walls of around 50-100nm thick [61].

The formation and motion of the domain walls is dependent on the size of the material. In Bulk materials the domain walls can rotate out of plane, perpendicular to the surface, known as Bloch walls. More relevantly, in thin films - where there is strong in-plane shape anisotropy - the moments rotate in-plane, known as Neel walls.

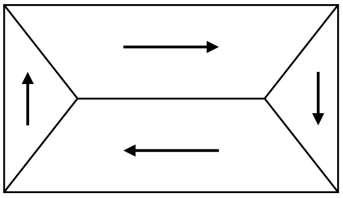

Figure 9: Diagram showing the structure of inner domains separated by Neel walls.

Crucially the domain structure has important consequences for manipulating macroscopic fields. By applying an external field, the domain walls can be shifted until the magnetisation is fully saturated. This theory was further supported by the discovery of Barkhausen noise in 1919, detailing the incremental changes in magnetisation deriving from shifting domain walls, and defects in the crystal structure [82]. There exists regions in the magnetic material which have different properties to the rest of the crystal, known as magnetic inclusions. The inclusions can be caused by defects and

APB's and create a resistance to the motion of domain walls. When domains are shifted and pass through these regions, they may undergo domain wall pinning to the inclusion; an external field is needed to overcome the barrier and unpin the domain wall. This phenomenon was fully explained by Landau and Lifshitz in 1935 when they showed that internal closed flux paths created by domains have lower energies [75]. They also described the motion of domain wall shifts, by the velocity of propagation of spin waves.

These investigations show that magnetic domains play a crucial role in the observation of macroscopic fields; ultimately being controlled by the shifting of domain walls.

2.6 Hysteresis

The effect of domain wall motion can be seen when a sample is introduced to an external magnetic field to obtain a hysteresis loop (figure 10). The resultant hysteresis loop is a measure of the magnetic susceptibility and responsiveness of a material. The applied field is swept such that it reaches the magnetic saturation (M_s) of the sample, then reduced to zero, to the magnetic remanence level (M_{rs}). The full loop is completed by sweeping the applied field, from positive to negative magnetic saturation. During this process the magnetic moments will be fully aligned in one direction and then rotated by 180°. The varying shapes of a hysteresis loop can reveal in-depth magnetic characteristics and structural properties of the sample.

Initially when a sample is placed in an applied field, the shifting domain walls need to overcome the pinning, causing a lag in the magnetisation. Afterwards, when the sample approaches magnetic saturation, there is a coherent rotation of the magnetisation, eliminating the domain microstructure. Coherent loop rotation is when the moments rotate with the field with a uniform magnitude of magnetisation. The subsequent magnetisation reversal process in hysteresis loops, is a complex phenomena, governed by many factors, such as the domain wall pinning, nucleation and coercivity. When the field decreases from saturation, the process of domain nucleation begins. This is when the material moves from a coherent state back to a multi-domain state; with newly formed domain walls propagating through the sample - overcoming the domain wall pinning - until it is fully demagnetised at H_c [43]. Coherent rotation and the motion of domain walls govern the magnetic response and determine the properties of the M-H loops.

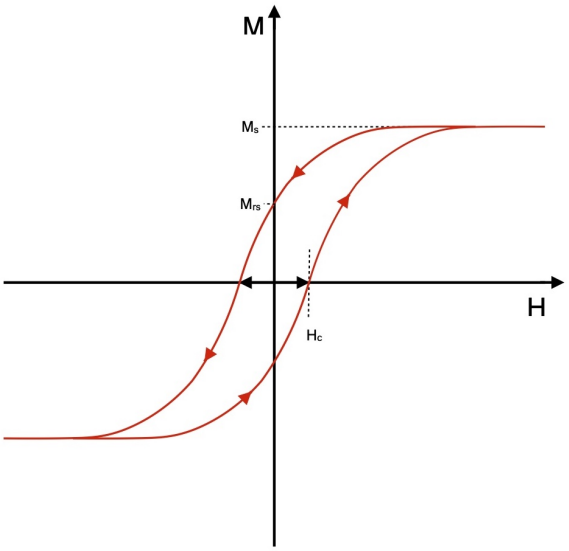

Figure 10: Example of a typical M-H loop.

By manipulating the magnetic moments and domain walls in this way, we can determine magnetic properties such as, magnetic coercivity, remanence and anisotropy contributions. The remanence of a magnetic sample is de ned as the resultant magnetisation in the absence of an applied eld, revealing the retentivity; how much magnetisation the sample can hold at zero eld. The magnetic coercivity, is the eld required to demagnetise the sample from saturation. The coercivity can be linked to the width of the loop, showing the magnetic history dependence of the sample. The thinner the loops the more responsive the magnetic moments are, continuously rotating with the eld.

Typically, magnets are de ned as either hard or soft, depending on there coercivity. A hard magnet will have a larger coercivity and will exhibit a broad square-like hysteresis loop; showing its high eld retentivity. Soft magnets have narrower loops, with a small coercive elds and remanence values. The ferromagnetic iron group elements are soft magnets and very responsive to applied elds.

3 Methodology

3.1 Pulsed Laser Deposition

In this thesis pulsed laser deposition lm growth is utilised for the growth of three di erent $NiFe_2O_4$ lms. This lm fabrication technique makes use of a high-powered UV laser directed at a target material held in a chamber (gure 11). Unlike other growth techniques,like MBE, the chamber does not need UHV conditions and can grow lms at higher pressures, making it more exible. The incident laser beam vaporises the target material sending a plasma plume towards the substrate. As a result, the lm growth is substantially quicker than MBE, taking minutes to reach the same thickness. Consequently, there is far less control in PLD growth, which is done by layer by layer growth. The ablation of the target completely destroys the surface and sends various ions and atoms in the plume. When the plums reaches the substrate, the atoms recombine, matching the phase of the target; this is known as the nucleation of the lm. During the process the substrate is heated by a CO_2 laser to temperatures of around 300°C, assisting the nucleation process. Papers such as (Zhou, He and Nan, 2007) have demonstrated the optimum conditions for PLD growth of the ferrites, using an oxygen chamber pressure of around 10^{-5} mbar [83]. One of the main advantages of PLD is that the ferrites can be deposited with the desired stoichiometries as the target [84].

In this study $NiFe_2O_4$ lms were grown by PLD on Al_2O_3, MgO and $MgAl_2O_4$ substrates. Before growth, the substrates are speci cally prepared by a cleaning procedure in an ultrasonic bath. This is performed by submerging the substrates in a beaker of acetone, isopropanol and nally deionised water for 15 minutes each. This three-step process removes any surface dirt and prepares the substrate to enter the chamber. The substrates are annealed to 1100°C for one hour before being loaded into the PLD chamber. The annealing removes any other remaining contaminants but most importantly it attens the surface before lm deposition.

An ultraviolet neodymium-doped yttrium aluminium garnet laser was used, with a wavelength of 266nm. The pulsed laser operates at a frequency of 10 Hz with a 2ns duration. The O_2 pressure in the chamber was held at $2x10^{-5}$ mbar with a laser power of 0.9W and the substrate heated to 350°C during growth. The growth time was held constant at 5 minutes.

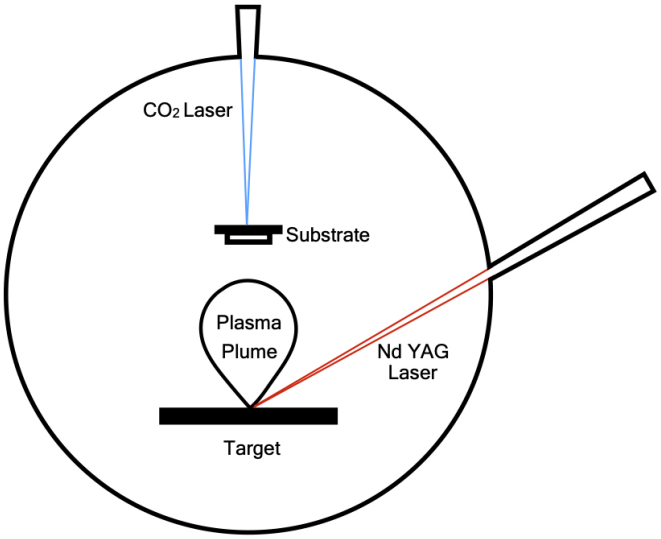

Figure 11: Schematic diagram of a PLD chamber.

3.2 Vibrating Sample Magnetometer

The vibrating sample magnetometer (VSM) is employed to determine magnetic characteristics by measuring a hysteresis loop. The sample is carefully tapped down to the end of a plastic rod, not to compromise the surface and inserted into the VSM. The rod is then lowered such that it is positioned between two electromagnets as shown in gure 12. VSM works by Faraday's Law (11); vibrating the sample between two electromagnets at a constant rate, whilst the applied magnetic eld is varied.

$$= N \frac{r}{r t} \tag{11}$$

When a sample is placed in a uniform magnetic eld, the sample is magnetised in accordance with its magnetic susceptibility. Therefore, the sinusoidal motion of the magnetised sample will induce a potential di erence, according to Lenz's law, into the pick-up coils. These pick coils are situated at the end of the electromagnets, with the gap between the sample and magnets as small as possible, optimising the signal from the thin lms. Changing the applied eld and subsequently the samples' magnetisation, we are able to measure the resultant variations of this induced emf. The induced electric eld is proportional to the changing magnetic eld which is used to determine the values of the magnetic moments. The emf signal from the pick-up coils is ampli ed and corrected via the VSM, converting to emu.

Before measuring, the VSM needs to be calibrated with respect to the gap between the electromagnets. A palladium control sample is used for calibration; the measured moment from the VSM is adjusted to align with its theoretical emu value. The signal is further optimised by altering the position of the sample in the x, y and z direction to nd the geometric centre of the pick-up coils. Sample saddling is used to determine the minima and maxima points, achieving the highest emu signal output.

Initially the applied eld is ramped up to saturate the magnetic moments in the sample such that they are all aligned parallel [85]. The eld is switched back to the initial value and the resultant applied eld-magnetisation graph gives a hysteresis loop.

In this thesis VSM is performed by varying the angle between the applied eld and sample plane (gure 13). This aims to give a holistic picture of the magnetic anisotropy and the changes in the switching eld distribution of the sample.

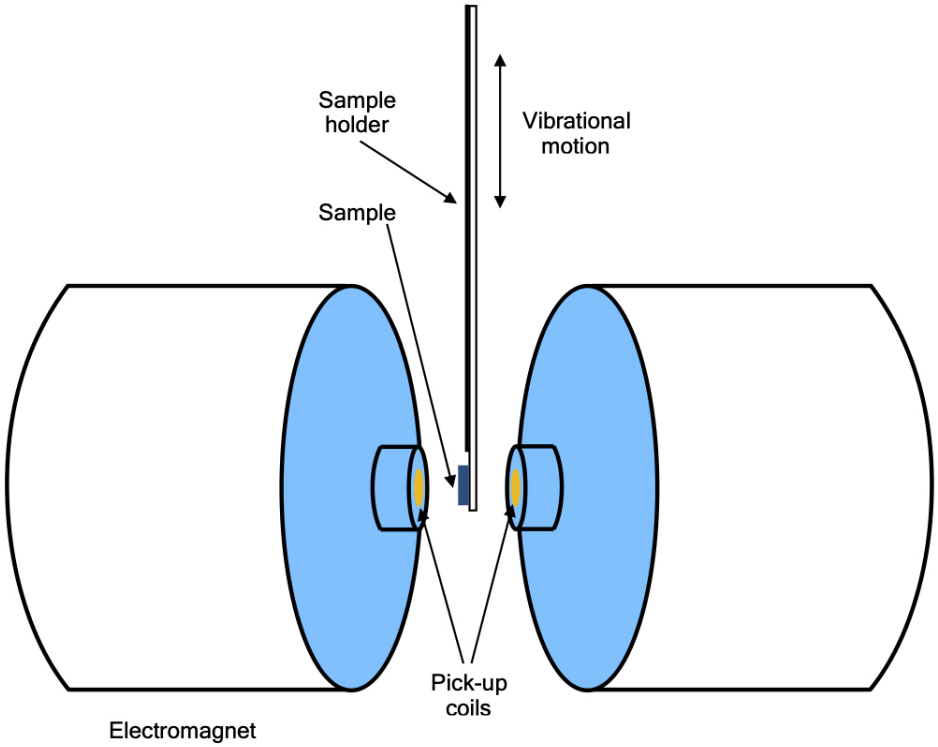

Figure 12: Schematic diagram of the VSM setup.

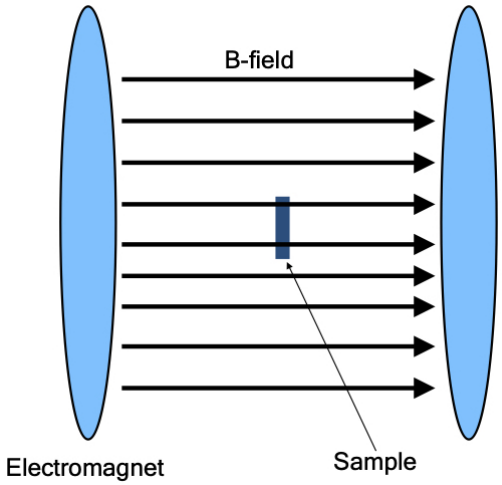

Figure 13: Birds-eye view of the sample normal (90°) to the applied eld.

3.3 X-ray Diffraction

X-ray di raction is an extremely powerful characterisation technique; frequently the rst method employed, to determine the crystallinity and crystallographic orientation of grown lms. X-rays are particularly useful as their wavelength is of a similar magnitude to the lattice spacing's, in order of Angstroms. This discovery by Max Von Laue in 1912, was of such signi cance that it earned him the Nobel prize in 1914 and brought about much interest in X-ray physics, most notably by W. L. Bragg [86]. XRD enables us to determine the periodic lattices of the single crystal structures; useful for lms grown in this thesis.

The nature of crystalline materials is characterised by the mathematical formulation of a Bravais lattice, mapping each lattice point in the structure; subsequently populated by a basis of atoms. This mathematical description of the atomic arrangements in crystals has an intrinsic relationship to X-ray di raction, being the di raction pattern of the lattice, known as the reciprocal lattice. The reciprocal lattice is a projection of the real-space Bravais lattice into momentum-space. Initially an abstract concept, it is critical for understating electronic motion through crystals, which lead to the concept of Bloch waves, again by utilising the periodicity of the lattice.

The simplest understanding of XRD proposed by Bragg, is that the incident X-rays are re ected o lattice planes, described by the Bragg's law (12) [87].

$$2d\sin(\ ) = n \tag{12}$$

As the X-rays penetrate through the successive crystal layers, the path di erence of re ected X-rays leads to the constructive interference measured by the detector (gure 14). The resultant X-ray peaks of the thin lms are used to nd the epitaxial growth orientation of the samples, with respect to the substrates. The simplicity of Bragg theory means that it does not account for the atomic arrangements on the lattice, but rather just the lattice itself, revealing no information about the samples' crystallography [88]. This is because the incident X-rays only interact with the lattice planes and not the constituent atoms. A more rigorous approach in understanding the data from XRD means a discussion of the physical interaction between the X-rays and crystal.

The X-rays' interaction is one of electromagnetic nature, between the charge densities of the atomic structure and the incident rays. The incoming X-rays excite the electrons via the Coulomb interaction, causing the electrons to oscillate. As a result, the accelerating electron becomes a source

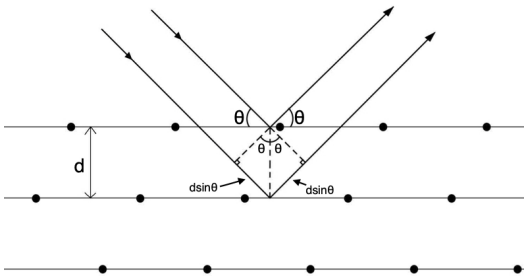

Figure 14: Diagram showing incident x-rays re ecting o lattice planes in accordance with Bragg's law.

of secondary photon emission of the same wavelength, in all directions, known as Thomson scattering [89]. Therefore, the results of XRD are heavily dependent on the atomic number of the elements involved; the higher the atomic number, the stronger the X-ray interaction with the sample. We assume elastic scattering for XRD, such that the incoming and outgoing wave vectors are of the same magnitude.

The amplitude of scattered X-rays, described by the atomic form factor, can result in X-ray interference as a function of incident angle [90]. This atomic form factor governs the interaction for di erent atoms with the incident X-rays, de ning a measure of the scattering amplitude of the outgoing wave vectors. Most importantly this gives rise to a mathematical formulisation for determining the structure factor. The structure factor is a cohesive measure of the interference patterns by the incident X-ray scattering. This is expressed by a summation of atomic form factors for each element across the lattice basis.

An important aspect of XRD is the determination of crystalline grains in materials. This is calculated by the Scherrer equation (13) which relates the full width half maximum ( ) of the peak to the crystallite size ( ). A broader XRD peak indicates smaller crystal grain sizes. For single crystal ultra-thin lms, the Scherrer equation isn't particularly relevant as we expect thin lms to have higher crystallinity.

$$= \frac{}{cos} \tag{13}$$

XRD line broadening can also occur due to defects or di erences in the lattice, epitaxial strain included. Large lattice strains will contribute to the FWHM of the peak, but this can also be a

contribution from the instrument, making it di cult to analyse. An analysis on the accuracy of the FWHM calculation of crystalline sizes and microstrain was carried out by (Bushroa et al., 2012) by way of comparing the results with a more rigorous Warren-Averbach method [91]. The FWHM can be somewhat unreliable depending on the signal to noise ratio and positioning of the peak, but (Bushroa et al., 2012) concluded that it is a suitable approximation [91].

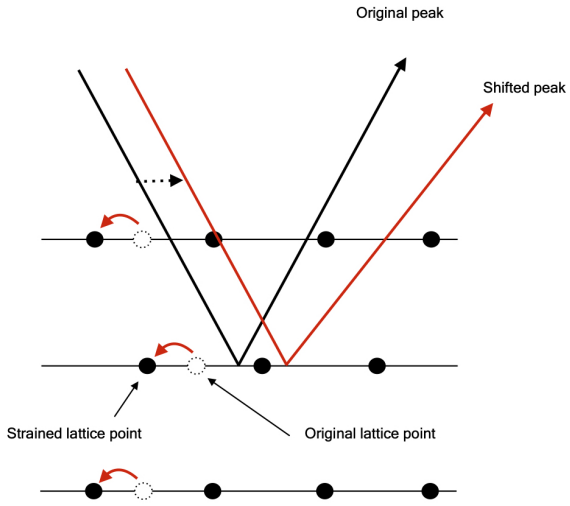

Figure 15: Diagram showing the XRD shift and peak broadening on a strained lattice in comparison to an unstrained lattice.

The collection of such detailed X-ray interactions, and with exploiting the symmetry of the lattice leads to a complete di raction pattern. This information is then related to the real space crystal via a Fourier transform.

3.4 Transmission Electron Microscopy

Microscopy has always been an important tool in the analysis of objects and phenomena unseen by the naked eye. Since the birth of quantum physics in the early 20^{th} century there has been a great demand to probe deeper into the atomic structure. The obvious problem is that optical microscopy is limited by the wavelength of light, of around 200nm; signi cantly larger than the atomic lattice spacings. Therefore, it is impossible to observe the crystal structure with light, another method had to be found. In 1924 Louis de Broglie proposed the theory of wave-particle duality, giving rise to a new form of microscopy, by using the apparent wavelength of electrons to `see' with a far greater resolution. The de Broglie wavelength is governed by (14) [92]. The greater the momentum, the smaller the wavelength.

$$= \frac{h}{p} \tag{14}$$

By using this relationship, Max Knoll and Ernst Ruska invented the rst ever electron microscope in 1931 [93]. One of the most profound inventions; it has given invaluable insight across all scienti c disciplines and was awarded the Nobel prize in 1986 [94].

As well as exploiting the electrons' small wavelength, the electromagnetic interactions with matter are useful for a variety of other techniques (gure 16). With electrons being a form of ionising radiation, and coupled with the high beam voltages required to achieve a higher resolution, there is a trade-o that needs to be established. For some forms of microscopy this can be a useful e ect; by exciting electrons from the inner K shell, they emit K alpha spectral lines (X-rays). This X-ray emission can be measured to perform chemical analysis to study composition via energy dispersive X-ray analysis (EDX). Furthermore, in SEM, secondary and back scattered electrons are utilised to acquire di erent information across a range of samples and electron voltages.

For TEM the direct transmission beam is the main source of imaging electrons. But how do these electrons create an image? TEM uses electrons that pass through the specimen to gain insight into atomic structure and chemical composition of thin lm specimens, by HRTEM, electron di raction and EDX and electron energy loss spectroscopy (EELS). The most important aspect of imaging is the di raction pattern, containing all the crystallographic information from the sample. This can be produced by a fast Fourier transform (FFT), a computational algorithm used to convert TEM images into reciprocal space. To appreciate this information we have to understand the journey of

the incident electrons through the specimen. Although there are two mechanisms for scattering - from both electrons and nuclei - the nuclei scattering dominates.

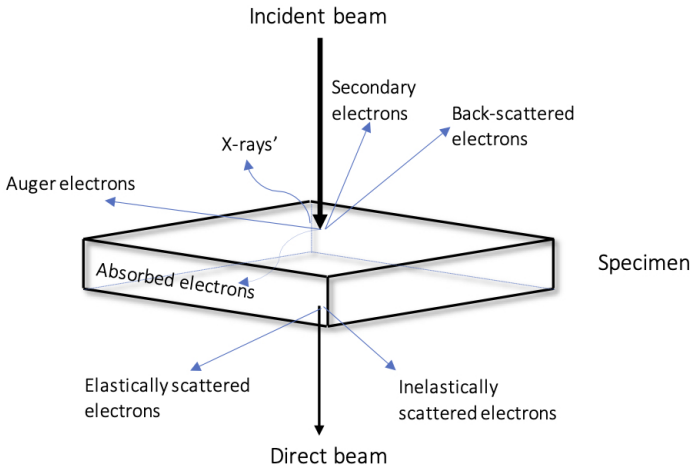

Figure 16: Diagram showing the signals emitted from di erent electron interactions with matter [95].

Scattering events from the nucleus are the main source of information allowing us to `see' the reciprocal lattice and thus the Bravais lattice. With a variety of scattering angles, it is a case of which electrons contribute to what information. Unlike XRD, the electrons' interactions are a product of wave-particle duality. We can categorise the scattering events into two phenomena, either elastic or inelastic collisions. In elastic collisions, the scattered wave vectors under low angle are coherent, as the angle increases, the coherency is lost. By contrast, inelastic collisions are mainly incoherent. These types of interactions show how both the wave and particle nature of the electrons are observed in electron microscopy. The coherent elastic scattering behaving more wave like, whereas the incoherent collisions are analogous to a more classical particle approach to scattering.

In these specimens, most electrons will pass through the sample with no interactions, but it is quite possible for there to be multiple collisions. The less scattering events that occur result in receiving more interpretable information from the specimen. We can assume that in TEM only one scattering event will occur, which is dependent on the specimen preparation. The thickness of the specimen is the main factor in reducing the number of scattering events and therefore, specimens with thicknesses below 100nm are required for TEM.

The characteristics of the specimen such as density, determine the distribution of scattering angles occurring from the di erent interactions. Therefore, it is necessary to formulate an idea for the likelihood of a scattering event, the scattering cross section, this determines the probability of a collision. It is possible to manipulate the scattering cross section *in situ*, commonly by the beam voltage; a higher beam voltage will reduce the probability of a collision. By integrating the di erential cross section, we can determine that there are fewer scattering events at higher angles normal to the direct transmission beam.

The elastically scattered electrons are de ected by maximum angles of 250 mrad, allowing them to pass through the aperture of the TEM. Crucially these are the electrons which provide the most crystallographic information. The di raction of the scattered electrons is analogous to Fraunhofer di raction, which occurs with plane waves at large distances (far eld di raction). Each aspect of the di raction pattern correlates to di erent information. The positions of the reciprocal lattice points reveal the structure of the unit cell and the relative intensities of the pattern is related to the basis and atomic structure inj kinematical approximation.

Upon interactions and scattering events, the transmission electron waves carry information via both amplitude and phase, both of which are crucial to imaging. Amplitude contrast is of particular importance due to the intensity changes and its implications [96]. The contrast of an image is de ned as the di erence of intensity across the sample. The origins of this change is due to the variations of specimen thickness and density.

3.4.1 Bright field dark field imaging

There are two main ways to condense and focus the transmission electrons to exploit the amplitude contrast e ect. These two types of imaging are called bright eld and dark eld TEM. For bright eld imaging the electrons are collected from the direct beam, those which have undergone no scattering events. Thus the `gaps' in the image from the lack of di racted electrons can be used to form an image. The converse is true for dark eld imaging; only the di racted electrons are detected and used for imaging. To speci cally detect these electrons requires a narrow aperture, which can result in some lost information.

In comparison to bright/dark eld imaging, high resolution TEM is another important mode for gathering TEM information, this captures all the electrons from the specimen.

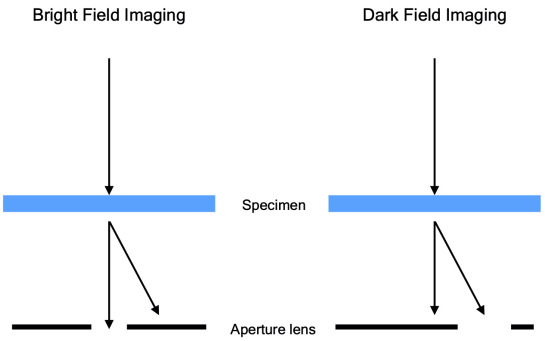

Figure 17: Schematic diagram showing which part of transmitted electrons are detected in Bright eld and Dark eld imaging.

Modern TEM's have a wide range of voltages and magni cations, with resolutions to the order of picometers. Due to the imaging process being a transmission of electrons through the sample, the resultant image is 2-dimensional projection of the 3D specimen. This adds another layer of complexity to the analysis of the specimen.

3.5 Sample Preparation

Before imaging, the sample must be carefully prepared in order to use TEM. The prerequisites for a good TEM specimen are a uniformly thin cross section of the sample as well as being partially conducting. The sample must be thinned substantially to achieve electron transparency, below 100nm in thickness, yielding the best TEM images. These preparation techniques of the specimens are crucial as they play a big part in the limiting factors to produce high resolution images. These techniques result in some degree of destruction, meaning that TEM specimens are only prepared after all other measurements have taken place.

In this thesis, TEM preparation is done in two di erent ways; by mechanical polishing and focused Ion beam milling (FIB). Both methods have their bene ts and drawbacks depending on the sample, timing and the data we want to gain from the TEM.

3.5.1 Mechanical Polishing

The mechanical preparation process is a relatively simple one, but very delicate and time consuming, especially with small samples of 5 x 5 mm. Producing a specimen ready for TEM is as follows: slicing the initial sample to form the specimen, polishing it down to a thickness of 0.1 mm and then nally ion milling a hole to electron transparency. The entirely of this process can take up to a week and with a small and limited amount of the sample, extreme care must be taken throughout the process.

The rst step consists of mounting the sample (interface down) onto a piece of glass and applying crystal bond wax. When placed onto a hot plate at 135°C, the wax will coat the sample and rmly adhere itself to the glass within a few minutes. At this stage we have to be mindful of the orientation and position we have glued the sample for the cutting process. The crystal bond should be liberally spread to make sure no part of the sample falls o the glass whilst cutting. Once the glass is taken o the hot plate the wax will solidify within minutes.

The glass slide is secured onto the cutting machine and aligned such that the saw is parallel to the edge of sample. Cutting is done by a thin diamond saw with light downward pressure keeping the blade straight and ensuring a sharp cut. The blade is set to the lowest angular velocity and